

Access to this work was provided by the University of Maryland, Baltimore County (UMBC) ScholarWorks@UMBC digital repository on the Maryland Shared Open Access (MD-SOAR) platform.

Please provide feedback

Please support the ScholarWorks@UMBC repository by emailing [scholarworks-group@umbc.edu](mailto:scholarworks-group@umbc.edu) and telling us what having access to this work means to you and why it's important to you. Thank you.

# Ultrastrong coupling of polar phonons and effective epsilon-near-zero modes in coaxial nanocavities

Daehan Yoo,<sup>1</sup> Fernando de León-Pérez,<sup>2,3</sup> In-Ho Lee,<sup>1</sup> Daniel A. Mohr,<sup>1</sup>  
Matthew Pelton,<sup>4</sup> Markus B. Raschke,<sup>5</sup> Joshua D. Caldwell,<sup>6</sup>  
Luis Martín-Moreno,<sup>3\*</sup> and Sang-Hyun Oh<sup>1\*</sup>

<sup>1</sup>Department of Electrical and Computer Engineering, University of Minnesota,  
200 Union St. S.E., Minneapolis, MN, USA,

<sup>2</sup>Centro Universitario de la Defensa de Zaragoza,  
Ctra. de Huesca s/n, E-50090 Zaragoza, Spain,

<sup>3</sup>Instituto de Ciencia de Materiales de Aragón and Departamento de Física de la Materia Condensada,  
CSIC-Universidad de Zaragoza, E-50009 Zaragoza, Spain,

<sup>4</sup>Department of Physics, University of Maryland, Baltimore County, Baltimore, MD, USA,

<sup>5</sup>Department of Physics and JILA, Department of Chemistry, University of Colorado, Boulder, CO, USA,

<sup>6</sup>Department of Mechanical Engineering, Vanderbilt University, Nashville, TN, USA.

\*E-mail: lmm@unizar.es and sang@umn.edu

**Ultrastrong coupling (USC), where the light-matter coupling strength is comparable to the resonance frequency of the uncoupled bare system, presents new frontiers in nanophotonics. However, it has remained notoriously difficult to achieve experimentally. Here we demonstrate USC between polar phonons and mid-infrared (MIR) light in coaxial nanocavities. We achieved a level splitting of strongly coupled polaritons of 50% of the resonant frequency, enabled by the effective epsilon-near-zero (ENZ) responses in the MIR of the SiO<sub>2</sub>-filled coaxial nanocavities. We theoretically describe this unusually large**

**level splitting as USC phenomenon using a  $2 \times 2$  matrix form derived from the coupling of polar phonon lattice and Maxwell's equations. Our wafer-scale coaxial ENZ nanocavity platform offers new routes to explore the physics of vibrational USC within polaritonic systems and harness a broad range of resonant transitions in the MIR regime.**

Traditionally, two regimes of light-matter interactions have been considered: weak coupling (WC, when losses exceed light-matter coupling strength) and strong coupling (SC, when coupling strength dominates) (1, 2, 3). In contrast to WC phenomena such as Purcell effect (4) and Fano interference (5), in the SC regime the oscillators can exchange their energy reversibly and coherently, generating hybridized modes with distinct energy levels and mode characteristics compared to those of the bare constituents (6, 7, 8, 9, 10, 11, 12, 13). Light-matter SC can lead to novel phenomena such as the modification of chemical reaction rate (14), suppressed photo-oxidation (15), enhanced exciton transport (16), and modification of ground-state reactivity (17). Furthermore, SC of optical fields and quantum emitters can be used as a basis for quantum information processing (18).

When the coupling strength (measured by the vacuum Rabi splitting,  $\Gamma$ ) of the system becomes comparable to the frequency of the material transition, new phenomena can occur. This is the so-called ultrastrong coupling (USC) regime (1, 2, 3, 19). In the USC regime, standard approximations based on weak perturbation may break down, so reaching this regime can both benefit fundamental studies of light-matter interactions and potentially lead to the development of novel photonic devices and sensors. For instance, quantum information processing, including ultrafast quantum gating in circuit-QED system (20) and quantum metrology with high-resolution spectroscopy (21), could be achieved via coherent energy exchange between light and matter. Also, USC between light and molecules can extend the ability to control chemical reactions in ways beyond what is possible in the WC and SC regimes (3). However, reaching

the USC regime has been notoriously difficult because it requires very large coupling strength (i.e., 10~20% of the frequency of the material transition). The conventional strategy to increase coupling strengths is to increase the number of transition dipoles involved in coupling with the photon while minimizing the mode volume (22, 23).

Among various spectral domains to explore the physics of USC, the mid-infrared (MIR) is of particular interest, since vibrational bands of many molecules reside in this regime (24), and enhancing their interaction with MIR light is highly desirable for spectroscopic applications (25, 26, 27), and surface-enhanced IR absorption spectroscopy (SEIRA) in WC (28, 29). Vibrational SC in the MIR regime has been demonstrated in boron nitride nanoresonators (30), for cavity-modified catalysis (31) and reaction-site selectivity (17), among others. However, pushing MIR light-matter interactions into the USC regime has so far proven elusive, due to the intrinsically weaker oscillator strengths for vibrational modes compared to those for electronic transitions in the visible regime. Further, at the long-MIR wavelength, surface plasmon waves are only weakly bound to metal surfaces, leading to significantly larger mode volumes.

Here we use coaxial nanocavities with only few-nm gaps to reach the vibrational USC in the MIR, as an enabling platform to enhance MIR-vibration interaction. The coaxial aperture with its strong resonance close to the cutoff frequency of the  $TE_{11}$  mode of the coax (32, 33), provides the diameter tunable spectra while maintaining mode confinement in the nanogaps.

We note that, for very narrow gaps,  $TE_{11}$  coax modes have a strong plasmonic character. Such modes are characterized by an effective dielectric constant which is approximately zero at cutoff. This resonance can be shifted toward longer wavelengths without sacrificing confinement (which is determined by the gap width) by increasing the coax diameter. In addition, the associated spatially uniform optical field, due to a very long wavelength at near-zero-permittivity provides the efficient coupling to the material and its resonances within the gaps. Using  $SiO_2$  as a representative phononic material, we demonstrate USC, exceeding 50% of the

resonant ENZ frequency.

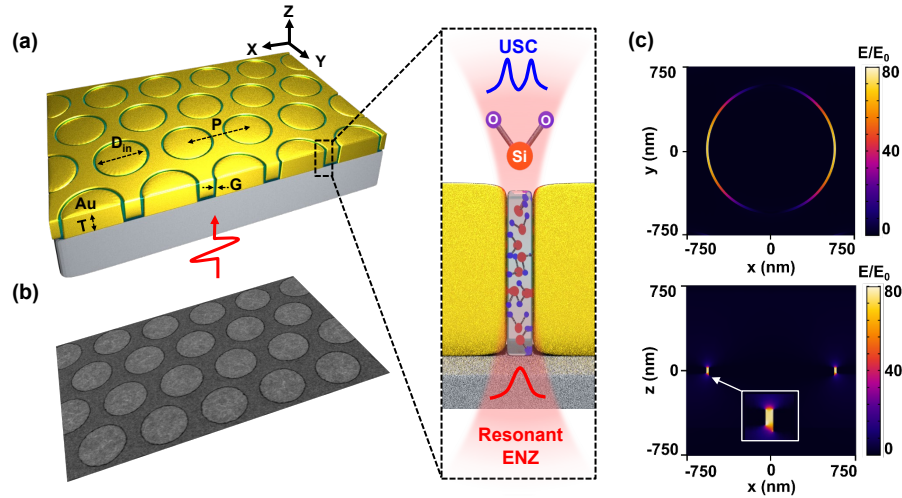


Figure 1: SiO<sub>2</sub>-filled coaxial nanocavities. (a) The illustration of coaxial nanocavities and geometrical parameters and showing how the SiO<sub>2</sub> phonon is interacting with ENZ mode in this system. (b) Scanning electron microscopy (SEM) images of coaxial nanoapertures with 21 nm gap, 790 nm diameter, 1190 nm period, and 80 nm Au thickness. (c) Computed electric field profiles of a coaxial nanocavity showing a lateral section (upper) and a vertical section (lower) of the ENZ transmission resonance.

The SiO<sub>2</sub>-filled coaxial nanoapertures in a metal film are hexagonally arranged with varied gap size ( $G$ ), diameter ( $D$ ), and lattice spacing ( $L$ ) (Fig. 1a,b). The array exhibits an optical transmission resonance near the cutoff frequency of the TE<sub>11</sub> mode, which can be understood both as an ENZ (34) resonance and as a zero-order FP resonance. The spatially coherent electric field profiles inside the gap associated to the ENZ resonance are shown in Fig. 1c. Importantly, the resonant frequency can be tuned by changing the geometry (diameter and gap width) of the coaxial apertures. Notice also that the cutoff resonance is a single-aperture effect, so the existence of an array is not essential for the transmission resonance we are considering (Sec.

S5).

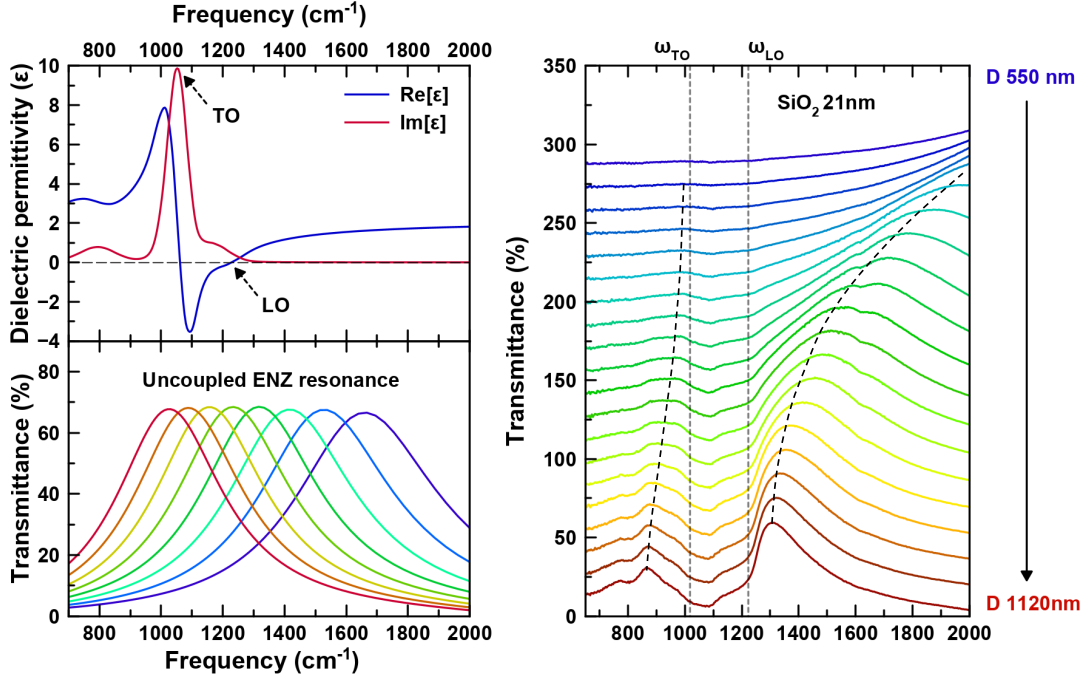


Figure 2: (a) Dielectric function (35) of  $\text{SiO}_2$  (top) and ENZ transmission resonances (bottom) of the coaxial nanoapertures ( $G = 21$  nm, diameter range: 700 to 1120 nm), simulated with a frequency-independent dielectric constant  $\epsilon_\infty$  inside the hole. This calculation shows that the bare (uncoupled to phonons) resonance sweeps the Reststrahlen band for the considered diameters (Sec. S2). (b) Normalized FTIR transmission spectra of  $\text{SiO}_2$ -filled coaxial Au nanocavities, for diameters ranging from  $D = 550$  nm to  $D = 1120$  nm. The coaxial gap is 21 nm. Black dashed lines are guides for the eye indicating the lower and upper polariton branches.

As shown in Fig. 2a, our coaxial nanocavities were designed to sweep the bare ENZ resonance across the Reststrahlen band defined by transverse optical (TO) and longitudinal optical (LO) phonons of  $\text{SiO}_2$  by increasing the diameter of each coaxial cavity. Plasmon-phonon inter-

actions were measured by far-field transmission measurements using Fourier transform infrared (FTIR) spectroscopy over a large-area chip. Measurements were made on 24 different arrays of coaxial nanocavities, whose diameter was varied from 430 nm to 1120 nm in steps of 30 nm. The normalized transmission spectra for coaxial nanocavities filled with 21 nm-thick SiO<sub>2</sub> are plotted with an offset along the y-axis corresponding to decreasing ring diameter (Fig. 2b). As the diameter is increased, its ENZ resonance frequency approaches that of the SiO<sub>2</sub> LO phonon. For D=640 nm, a small feature emerges near 1000 cm<sup>-1</sup> due to the coupling between ENZ photon and the IR-active TO phonon mode. By increasing the diameter, the ENZ resonance of the bare coaxial hole approaches  $\omega_{LO}$  (Fig. 2(a)). In this process, the transmission amplitude of the resonances increases while their linewidths decrease. For  $D = 1060$  nm and larger values, two separate modes are clearly identified, one below and one above the Reststrahlen band. At  $D = 1120$  nm, when the bare mode has already crossed the Reststrahlen band, they occur at  $\omega_- = 876$  cm<sup>-1</sup> and  $\omega_+ = 1310$  cm<sup>-1</sup>, showing a splitting normalized to the central frequency of 50%.

The electromagnetic propagation in waveguides is usually based on a description where the phononic degrees of freedom have been integrated out, providing an effective medium  $\epsilon(\omega)$  for the propagation of the photon (Sec. S6). However, for analyzing whether the system is in the strong coupling regime, it is convenient to retain both phononic and photonic degrees of freedom, in order to see whether there is coherent energy interchange between the two systems. For that, we consider a given waveguide mode M, characterized by a wavevector along the waveguide axes  $\mathbf{k}$  (for instance M=TE<sub>11</sub>, the fundamental mode of the coaxial waveguide). When the aperture is filled with a uniform dielectric constant  $\epsilon_\infty$  (originating from coupling to electronic degrees of freedom), the electric field,  $\mathbf{E} = E\mathbf{E}_M$ , satisfies the wave equation

$$\nabla \times \nabla \times E\mathbf{E}_M - \epsilon_\infty \frac{\omega_k^2}{c^2} E\mathbf{E}_M = 0, \quad (1)$$

where  $E$  is the field amplitude and  $\mathbf{E}_M$  is a transverse solution of Maxwell equations (Sec. S3). Following Born and Huang (36), when the phononic material fills the waveguide we assume a local relation between the electric field and the relative displacement of ions,  $\mathbf{x}$ . Then, for a given mode profile,  $\mathbf{E}(\mathbf{r}) = E \mathbf{E}_M(\mathbf{r}, k)$  and  $\mathbf{x}(\mathbf{r}) = x \mathbf{E}_M(\mathbf{r}, k)$ , with

$$\ddot{x} = \gamma_{11}x + \gamma_{12}E, \quad (2)$$

$$P = \gamma_{12}x + \gamma_{22}E. \quad (3)$$

where  $P$  is the amplitude of polarization vector  $\mathbf{P} = P \mathbf{E}_M$ ,  $\gamma_{11} = -\omega_{TO}^2$ ,  $\gamma_{12}^2 = \omega_p^2 \epsilon_\infty / 4\pi$ ,  $\gamma_{22} = (\epsilon_\infty - 1) / 4\pi$ , and  $\omega_p^2 = \omega_p^2 - \omega_{TO}^2$  (Sec. S6). Notice that  $\epsilon_\infty$  incorporates the effect of the electronic resonances excited at higher frequencies. The wave equation becomes, in this case,

$$\nabla \times \nabla \times E \mathbf{E}_M - \frac{\omega^2}{c^2} (E + 4\pi P) \mathbf{E}_M = 0. \quad (4)$$

By inspection, we find that  $\mathbf{E}_M(\mathbf{r}, k)$  satisfies Eq. (4) if  $\omega^2(E + 4\pi P) = \omega_k^2 E$  (strictly speaking, we are neglecting the variation between  $\omega$  and  $\omega_k$  in the impedance of the metal surrounding the waveguide, for a deeper analysis of how this affects the cutoff condition, see Secs. S4 and S5). This condition, together with Eqs. (2,3) can be expressed in a matrix form, stating that  $\mathbf{E}_M(\mathbf{r}, k)$  is still a solution of Maxwell equations but at a frequency  $\omega$  satisfying (see Sec. S7 for a detailed derivation and further analysis)

$$\begin{pmatrix} \omega^2 - \omega_{TO}^2 & \omega \omega_p \\ \omega \omega_p & \omega^2 - \omega_k^2 \end{pmatrix} \cdot \begin{pmatrix} \omega x \\ \sqrt{\epsilon_\infty / 4\pi} E \end{pmatrix} = 0, \quad (5)$$

Eq. 5 is one of the central results of our work. It shows that the dynamics between the vibrations and the electromagnetic field is controlled by a  $2 \times 2$  matrix similar to that used to discuss strong coupling. The main difference is that the off-diagonal elements acquire a linear dependence on frequency. This is not very relevant when analyzing anti-crossings, which focus on a narrow frequency range, but it is essential to understand the presence of an energy gap in the spectrum



i.e., the fact that the low-frequency asymptote of the upper polariton and the high-frequency asymptote of the lower polariton do not coincide as shown in Fig. 3a for the case of polaritonic bands in bulk SiO<sub>2</sub>. Notice that the simpler coupled harmonic oscillator model (Sec. S11), which is customarily used for fitting experimental data, does not show the  $\omega$ -dependence of the off-diagonal terms and therefore cannot describe the polaritonic branches correctly (cf. Figs. 3a and S7). Strong coupling in the presence of losses and additional vibrational modes are discussed in Secs. S7 and S8.

To summarize the new features of our theoretical framework: (i) Eq. 5 can be applied to homogeneous materials, waveguides, and cavities (Secs. S7-S9); (ii) while the previous analysis computed the effective dielectric constant, we kept the vibrational degrees of freedom, which allowed us to unambiguously interpret the results as SC; and (iii) our  $2 \times 2$  matrix is slightly different from the widely used one in terms of  $\omega$ -dependence. Although the phenomenology presented in Fig. 2(b) suggests the existence of strong coupling, other interpretations cannot in principle be ruled out. For instance, the appearance of the split transmission peaks could be due to a single wide transmission resonance being quenched in a central frequency range by the strong vibrational absorption close to  $\omega_{TO}$ , i.e., vibrations could work as a bandstop filter. However, our theoretical analysis clarifies this conceptually confusing situation (i.e. absorption vs. USC) that can often arise in the interactions of MIR light and polar materials using a mathematically consistent, and intuitive way that can reveal the nature of the USC interactions.

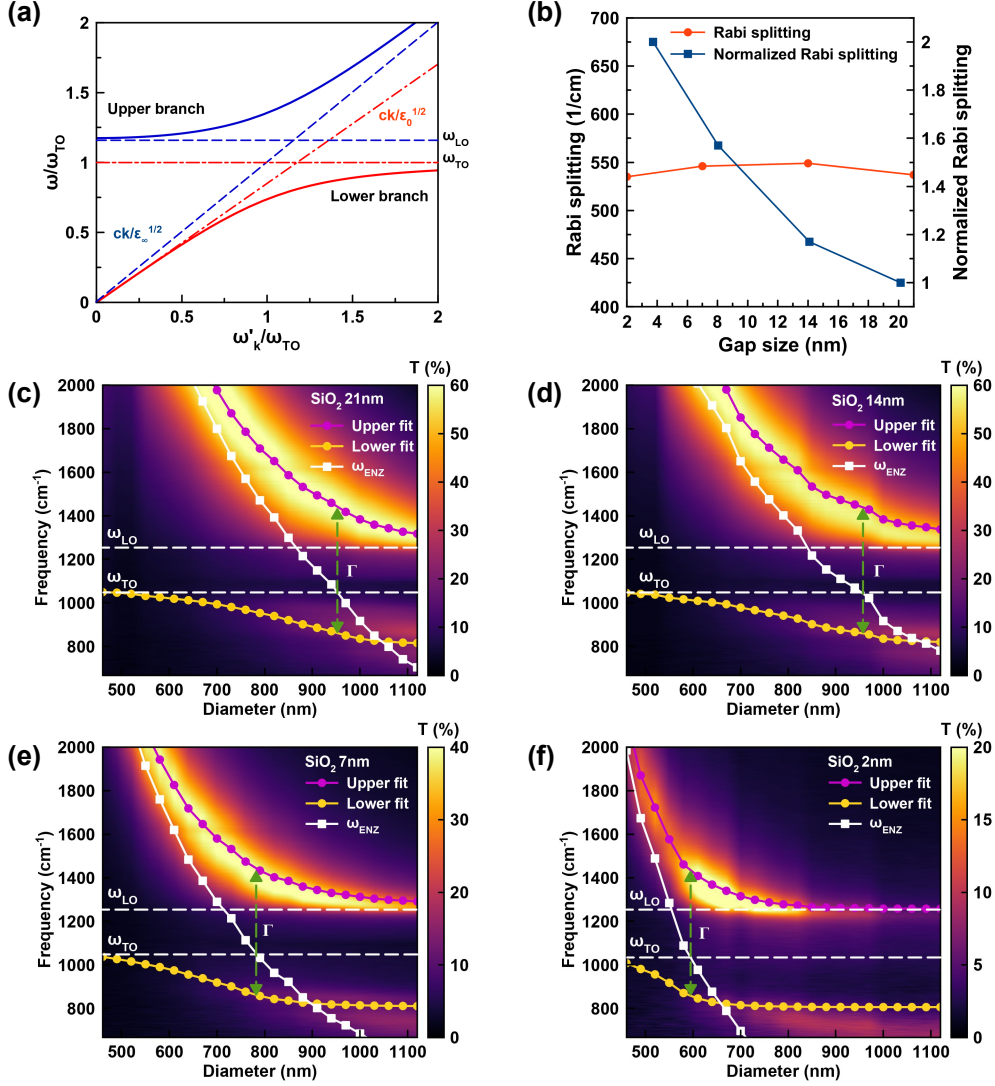


Figure 3: (a) Dispersion relation of bulk phonon polaritons in SiO<sub>2</sub> calculated by Eq. 5 assuming that a single vibrational mode is excited. (b) Rabi splitting and the gap volume as a function of the gap size. Dispersion maps of experimentally measured transmission spectra from coaxial apertures filled with SiO<sub>2</sub> film thicknesses of (c) 21 nm, (d) 14 nm, (e) 7 nm, and (f) 2 nm. Analytical fitting of polaritonic resonances using Eq. (S11) (black square dots with solid white line).  $\omega_{ENZ}$  (white circle dots with a solid black line) is used for fitting a parameter and indicates the resonance of the ENZ mode uncoupled with polar phonons of SiO<sub>2</sub>. Rabi splitting ( $\Gamma$ ) is measured at the intersection between the uncoupled ENZ resonance and the TO phonon frequency (when the detuning is zero).

Eq. 5 can be used to analyze the dependence of the ENZ resonant frequencies on the diameter of the coaxial hole. As  $\omega_p$  is independent of the hole shape and size, in strong coupling the ENZ resonances only depend on the bare ENZ,  $\omega_{ENZ}(D)$ . This process has been followed in Figs. 3c-f, which show the dispersion of the measured transmittance resonances for a series of coaxial nanocavity samples of varying diameters, with each sample featuring one of four different thicknesses (2, 7, 14, 21 nm) for the gap-filling  $\text{SiO}_2$ , together with the estimated theoretical values obtained from our model (Eq. 11 in S8). In fact, the parameter  $\omega_{ENZ}(D)$  was obtained from the upper polariton band (Sec. S10), and the model provides the estimate for the lower polariton band (notice that Eq. 5 predicts a Rabi splitting equal to  $\omega_p$  (Sec. S7) when only one vibrational mode is at play. We find that additional vibrational modes (included in Eq. S11 of Sec. S8) mainly affect the lower band and reduces the expected Rabi splitting). This procedure was followed because the lower polariton is more affected by additional vibrational resonances that have not been considered in this simple analysis. As the gap size is reduced from 21 nm to 2 nm, the lower branch of the hybrid mode observed below  $\omega_{TO}$  is pushed further toward lower frequencies, while the upper branch mode (above  $\omega_{LO}$ ) is pinned at  $\omega_{LO}$ .

For each value of the gap size, we estimate the Rabi splitting of the ENZ mode as the frequency difference between upper and lower polariton branches when  $\omega_{ENZ}(D) = \omega_{TO}$ , summarized in Table I. Although the linewidth of the uncoupled ENZ resonance at zero-detuning cannot be measured, we take advantage of its small dependence on hole diameter and, for each gap size, and estimate its value from ENZ resonances occurring at higher frequencies (where they do not couple with phonon modes). Results for both Rabi splittings and linewidths are tabulated in Table 1. All the cases exhibit mode splitting larger than the average of the linewidths of both the bare cavity resonance and the damping constant ( $77 \text{ cm}^{-1}$ ) of the oscillator at the TO phonon. Indeed, the coupling strength ( $\Gamma$ ), equal to the Rabi splitting, remains constant as the gap size (the cavity mode volume  $V$ ) is decreased from 21 nm to 2, as shown in Fig. 3b.

For SC involving a single dipole emitter, the coupling strength,  $\Gamma$ , is proportional to  $1/\sqrt{V}$ . However, in the case of collective SC,  $\Gamma$  is independent of the cavity volume, because in the cavity fully filled with vibrational dipoles the collective coupling strength  $\Gamma \sim \omega_p$  only depends on the density of molecules ( $n$ ) according to  $\omega_p = \sqrt{4\pi n e^2 / M}$ , where  $n = N/V$  (see Sec. S6).

However, we can see the different dependence of the coupling strength on the gap size through the normalized Rabi splitting defined by the ratio of the Rabi splitting to the average in bare ENZ and TO phonon linewidth. As shown in Fig. 3b and Table 1, the normalized Rabi splitting is increased as the gap size decreases, which arises from the linewidth reduction of bare ENZ resonance as the gap size shrinks.

Next, we calculate the normalized coupling strength ( $\eta$ ), the ratio of Rabi splitting to the phonon mode frequency. When the normalized coupling strength ( $\eta$ ), exceeds  $0.1 \sim 0.2$ , it can be said that the system is in the USC regime. As observed in Fig. 3 and Table 1, the SiO<sub>2</sub>-filled coaxial nanocavities show  $\eta > 0.5$  regardless of the gap width ranging from 21 nm to 2 nm, indicating that the USC regime is reached. Interestingly, linewidth narrowing of the coupled modes is observed in the SiO<sub>2</sub>-filled coaxes, compared to the bare cavity resonances (Figs. S2 and S3). The hybridized modes exhibit plasmon- and phonon-like optical properties simultaneously, resulting in linewidths that are the average of the plasmon and phonon modes. While uncoupled ENZ modes usually exhibit a quality factor ( $Q$ ) of  $2 \sim 3$  in the MIR regime, the hybrid mode generating in the vicinity of the asymptotic limits of LO phonon exhibits  $Q > 5$  for 2 nm-wide coaxes (Table S1).

SiO <sub>2</sub> gap (nm)	2	7	14	21
Bare ENZ mode Linewidth (cm <sup>-1</sup> )	453	619	844	990
Average in bare ENZ and TO phonon linewidth (cm <sup>-1</sup> )	265	348	481	534
Rabi splitting, $\Gamma$ (cm <sup>-1</sup> )	534	546	549	537
Normalized Rabi splitting: $\Gamma$ to the avg. in bare ENZ and TO phonon linewidth	2.02	1.57	1.14	1.01
Normalized coupling strength ( $\eta$ ): $\Gamma$ to the center frequency of TO	0.508	0.519	0.522	0.510

Table 1: Rabi splitting and the normalized coupling strength.

In summary, we have demonstrated USC between SiO<sub>2</sub> phonons and ENZ modes in resonant coaxial nanocavities. By harnessing the precision of the atomic layer deposition process, we could produce resonant nanocavities with the SiO<sub>2</sub> gap size down to 2 nm over an entire 4-inch wafer. This leads to a large mode splitting, with a normalized coupling strength ( $\Gamma$ ) greater than 0.5, originating from the interaction of the ENZ mode with SiO<sub>2</sub> TO phonons in ultranarrow cavities. Our coaxial nanocavity can be filled with a wide range of molecules, phononic or polaritonic materials. The ability to reach the USC regime in mass-produced nanocavity systems can open up new avenues to explore non-perturbatively coupled light-matter systems, multiphoton effects, as well as higher-order nonlinear effects (37), which may lead to novel applications in sensing, spectroscopy, and nanocavity optomechanics.

**Acknowledgments.** D.Y. and S.-H.O. acknowledge support from the National Science Foundation (ECCS 1610333). F.dL.P. and L.M.M. acknowledge financial support from Spanish Ministry of Economy and Competitiveness through projects MAT2017-88358-C3-1-R and MAT2017-88358-C3-2-R and the Aragón Government project Q-MAD. J.D.C. was supported by Office of Naval Research Grant N00014-18-12107.

**Competing interests:** The authors declare no competing interests

## Supporting Information

### S1 Device fabrication

Undoped double-side-polished 4-inch (100) Si wafer (University wafer) was spin-coated with AZ MIR701 photoresist for 45 s at 5,000 r.p.m. after pre-cleaning and pre-baking (200 ° C for 3 min) processes, then baked at 90 °C for 90 s. The patterns of hexagonal hole arrays with 24 different diameters from 430 nm to 1120 nm were transferred onto a Si wafer substrate by photolithography (Canon 2500 i3 stepper) with a dose of 150 mJ/cm<sup>2</sup> and the following post-exposure bake at 110 ° and development process with AZ 3000 MIF for 60 s. Hexagonal Au disk arrays were created on the Si substrate via directional evaporation of 3 nm Ti and 150 nm Au films (CHA, SEC 600) and the following lift-off process with AZ kwik strip. After oxygen plasma cleaning (STS, 320PC) with 100 W for 30 s to remove resist residue, the Au disk arrays formed on the Si substrate were coated uniformly with a thin SiO<sub>2</sub> film using ALD (Cambridge Nano Tech Inc., Savannah) at a typical deposition rate of 1.2 Å per cycle which was performed using ozone precursor and water vapor at 180 °. After the conformal sputtering of 3 nm Ti and 400 nm Au (AJA, ATC 2200), the top bumpy surface of 400 nm-thick Au-deposited disk patterns was planarized by an Ar ion beam of 240 mA at a 5 ° incidence angle from the horizontal plane of a substrate (Intlvac, Nanoquest) until the top entrance of coax MIM nanocavities is opened.

### S2 Comparison of simulations and experiments

To further investigate the coupling between ENZ and SiO<sub>2</sub> phonon modes, we compare FEM numerical modeling (dispersion map) and experimental results (white dots) in Fig. S1. FEM-modeled dispersion agrees well with the measured data, and we observe an anti-crossing band that is about two times wider than the Reststrahlen band. White circular dots are extracted from

the resonance peaks at the higher-frequency-side. White square dots trace the resonance peaks at the lower-frequency-side, below the TO phonon resonance of SiO<sub>2</sub>. This mode splitting in excess of the Reststrahlen bandwidth results in an unusually large forbidden energy gap compared with other strong coupling experiments involving phonon polaritons and MIR plasmonic resonators.

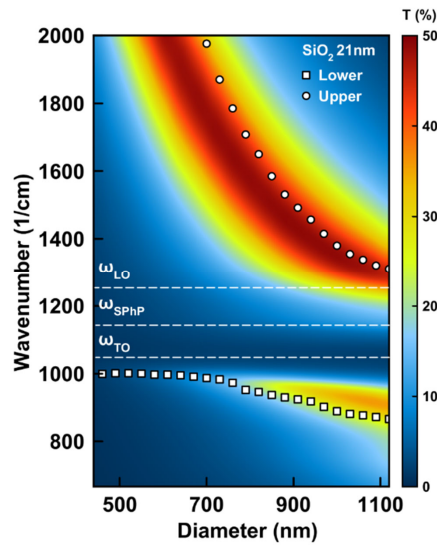


Figure S1: Color map shows simulated transmission spectra of coaxial nanoapertures (21 nm SiO<sub>2</sub> gap) in a gold film as a function of the coax diameter. White circular (square) dots indicate the upper (lower) branch spectral peak positions measured from FTIR spectra in Fig. 2b.

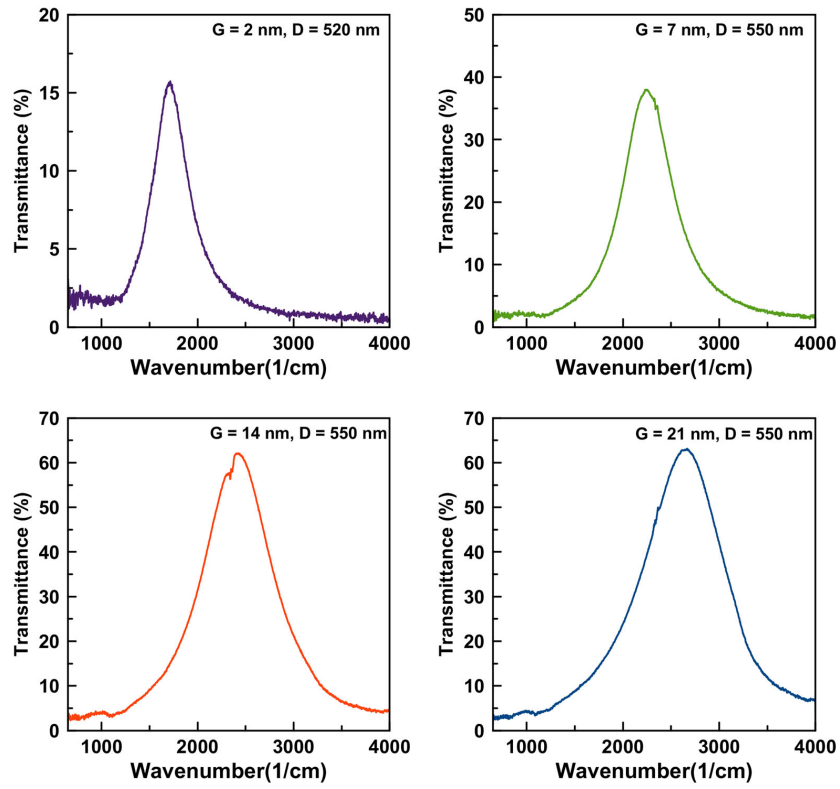


Figure S2: Resonance spectra used for measuring the linewidth of bare ENZ resonance.



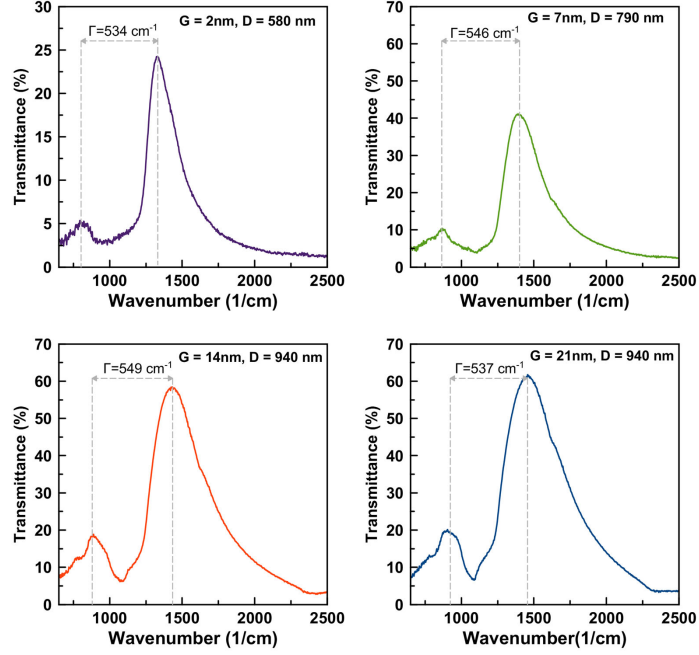


Figure S3: Resonance spectra used for measuring both the linewidth of coupled ENZ resonance and the resulting mode splitting.

Gap (nm)		2	7	14	21
Bare ENZ mode	Diameter (nm)	520	520	550	550
	Linewidth ( $\text{cm}^{-1}$ ) (Q factor)	453 (3.8)	619 (3.6)	844 (2.9)	990 (2.7)
At zero-detuned	Diameter (nm)	580	790	940	940
	Linewidth ( $\text{cm}^{-1}$ ) (Q factor)	245 (5.4)	312 (4.5)	438 (3.3)	483 (3.0)
Mode splitting ( $\text{cm}^{-1}$ )		534	546	549	537

Table S1: Measured linewidths of resonances shown in Figs S2 and S3

### S3 Wave equation

Wave equations (1) and (4) given in the main text have been derived from Maxwell's equations (Gaussian convention) (38),

$$\nabla \times \mathbf{H} = \frac{1}{c} \frac{\partial \mathbf{D}}{\partial t}, \quad (\text{S1})$$

$$\nabla \times \mathbf{E} = -\frac{1}{c} \frac{\partial \mathbf{H}}{\partial t}, \quad (\text{S2})$$

in the following way. After assuming harmonic solutions ( $\sim \exp(-i\omega t)$ ), we can apply the operator  $\nabla \times$  on (S2) and replace (S1) into the resulting equation to have

$$\nabla \times \nabla \times \mathbf{E} - \frac{\omega^2}{c^2} \mathbf{D} = 0. \quad (\text{S3})$$

Using the constitutive relation for the displacement current  $\mathbf{D} = \mathbf{E} + 4\pi\mathbf{P} = \epsilon\mathbf{E}$ , we obtain Eqs. (1) and (4) of the main text.

### S4 Scaling relation

At a given frequency  $\omega$  and for a general dielectric constant  $\epsilon(\mathbf{r})$ , the wave equation for the Electric field (S3),

$$\nabla \times \nabla \times \mathbf{E}(\mathbf{r}) - \epsilon(\mathbf{r}) \frac{\omega^2}{c^2} \mathbf{E}(\mathbf{r}) = 0, \quad (\text{S4})$$

only depends on the combination  $\kappa^2(\mathbf{r}) \equiv \epsilon(\mathbf{r})(\omega/c)^2$ . For a waveguide defined by an internal dielectric region (characterized by  $\epsilon_d$ ) and an external metallic region (with  $\epsilon_m$ ), the field only depends on the values of the corresponding  $\kappa_d^2$  and  $\kappa_m^2$ . The scaling relation

$$\epsilon_d, \epsilon_m, \omega \rightarrow \epsilon_d \eta, \epsilon_m \eta, \omega / \sqrt{\eta}$$

leaves  $\kappa_d^2$  and  $\kappa_m^2$  unchanged for any  $\eta$ . However, in general, for a given metal defining the waveguide, if the material inside the waveguide, is replaced by a different dielectric, the scaling

relation will not be fulfilled, so it is not possible to relate the dispersion relations of waveguide modes in these two instances. Nevertheless, we find two relevant exceptions: a perfect electrical conductor and a Drude metal at low frequencies.

In a PEC,  $\epsilon_m = -\infty$ . In that case, the dependence on  $\epsilon_m$  disappears from the scaling relation (as  $\epsilon_m \eta = -\infty$ , independent of  $\eta$ ). If Eq. (S4) holds and the waveguide is filled with  $\epsilon'_d(\omega)$ , the EM fields satisfy the same Maxwell's equation with  $\kappa_d'^2 = \epsilon'_d(\omega)(\omega/c)^2$  so that the solution  $\mathbf{E}$  for  $\epsilon_d$  at a given frequency  $\omega$  is the same than for  $\epsilon'_d(\omega')$  at a different  $\omega'$  given by

$$\epsilon'_d(\omega')\omega'^2 = \epsilon_d\omega^2. \quad (\text{S5})$$

A similar behavior is found for a Drude metal with dielectric function  $\epsilon_m(\omega) = 1 - \omega_{pm}^2/\omega^2$ . At frequencies much smaller than the plasma frequency  $\omega_{pm}$ , i.e. at MIR and smaller frequencies,  $\kappa_m^2 \approx -\omega_{pm}^2/c^2$  and does not depend on  $\omega$ . Therefore, field patterns only depend on  $\omega_p$  and  $\kappa_d^2$ . These trends are observed for the spectral window considered in the experiments.

In particular, Eq. (S5) is fulfilled when the field pattern corresponds to the cutoff condition  $k_z^2 = 0$ , where  $k_z$  is the component of the wavevector along the waveguide ( $z$ ) axis. Thus, if we know the cutoff frequency  $\omega_{c_\infty}$  when a waveguide is filled with a material characterized  $\epsilon_\infty$ , we can obtain the cut-off frequency when the material filling the waveguide is characterized by a dielectric constant  $\epsilon(\omega)$ :

$$\epsilon(\omega_c)\omega_c^2 = \epsilon_\infty\omega_{c_\infty}^2. \quad (\text{S6})$$

In fact, in the case of the strong frequency dependence of some dielectrics in the region of anomalous dispersion, this equation may have more than one solution (see below, when we will find instances when two solutions appear, which will be denoted  $\omega_+$  and  $\omega_-$ ).

## S5 Transmission resonances of a hole array

Modes in coaxial holes perforated in a metal film can be written as a linear combination of two counter-propagating waveguide modes with propagation constant  $\pm k_z$ . The bouncing back and forth of the EM fields inside the holes leads to Fabry-Perot (FP) like transmission resonances of the hole array. In particular, one such resonance appears spectrally close to the cutoff condition of the fundamental waveguide mode inside the hole (39), when the hole acts as an epsilon-near-zero medium. When holes are arranged periodically, additional transmission resonances appear at wavelengths slightly redrafted with respect to the array periodicity ( $P$ ), due to the excitation of surface modes. A strong hybridization of these two kind of transmission resonances occurs when the cutoff wavelength of a FP resonance is near  $P$ . However, our coaxial arrays are designed so that FP transmission resonances appear in the mid IR while surface resonances at the near IR, so that FP and surface modes do not hybridize.

Fig. S4 compares the transmittance of the hole array with the square effective index  $q_z^2 = c^2 k_z^2 / \omega^2$ . Notice that  $\text{Im}[k_z^2]$  does not vanish at cutoff due to the absorption losses. Even when the hole is filled with a lossless medium with dielectric constant  $\epsilon_\infty$ , losses in the metal cause that  $\text{Im}[k_z^2] \neq 0$ , see magenta line in Fig. S4. Despite absorption losses, Eq. S6 predicts the right cutoff frequencies using  $\omega_{c_\infty}$  as input parameter. The cutoff frequencies are represented with vertical dash-dotted lines in Fig. S4.

Finally, it is worth to notice that, in some of the structures we consider, the gap size (between  $G = 2$  and  $G = 21$  nm) is smaller than the skin depth ( $\sim 30$  nm). In these instances, the PEC approximation fails and the field profile and dispersion relation strongly depend on the penetration inside the metal, which thus must be taken into account in the calculation. Then, the fundamental waveguide mode has no longer a pure TM or TE character (as it occurs for a PEC), being instead a linear combination of the two polarizations. However, for the process of

transmission and the range of frequencies considered, we find that the TE component couples to the external illumination much better than the TM one, so the mode behaves effectively as a quasi-TE mode.

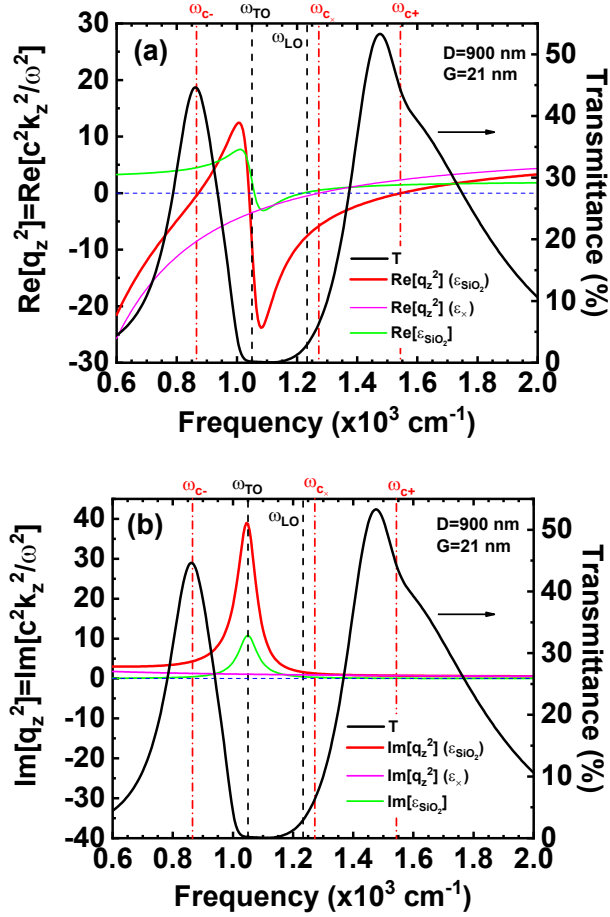


Figure S4: (a) Real and (b) imaginary parts of the squared effective index,  $q_z^2$  (red line), of the fundamental mode  $\text{TE}_{11}$  as a function of a frequency for a  $\text{SiO}_2$  filled coaxial gap with diameter  $D = 900 \text{ nm}$  and gap size  $G = 21 \text{ nm}$ . This quantity is compared with  $q_z^2$  for a  $\epsilon_\infty$  filled gap (magenta line) and the dielectric constant of  $\text{SiO}_2$  (green line). The cutoff frequencies (red dash-dotted vertical lines) of the  $\text{SiO}_2$  filled gap are computed with Eq. (S6). The transmittance for a hexagonal hole array with  $1190 \text{ nm}$  period, and  $80 \text{ nm}$  Au thickness (black line) shows peaks when hole are at cutoff, i.e. for  $\text{Re}[q_z^2] = 0$ . The coupled-mode method was employed for computing the transmission spectrum (40).

## S6 Lattice model for a homogeneous medium

For completeness, this section summarizes the theory developed by Huang (41) on the optical phonons in a diatomic crystal. In this case, there are three optical phonon branches (one longitudinal and two transversal). Unit cells with a larger number of atoms ( $s$ ), and correspondingly  $3(s - 1)$  optical branches, will be discussed in Sec. S8. For polarizable (nonrigid) ions in the diatomic cell the equation of motion and the polarization are given by

$$\begin{aligned}\ddot{\mathbf{x}} &= \gamma_{11}\mathbf{x} - \gamma_{12}\dot{\mathbf{x}} + \gamma_{13}\mathbf{E}, \\ \mathbf{P} &= \gamma_{13}\mathbf{x} + \gamma_{22}\mathbf{E},\end{aligned}$$

where the normalized coordinate  $\mathbf{x} = (\mathbf{u}_+ - \mathbf{u}_-)/\sqrt{\mu n}$  depends on the relative displacement of the positive and negative ions,  $\mathbf{u}_+ - \mathbf{u}_-$ , the reduced mass,  $\mu = m_+m_-/(m_+ + m_-)$ , and the number of cells per unit volume,  $n$ .  $\mathbf{P}$  and  $\mathbf{E}$  are the dielectric polarization and electric field, respectively. By considering harmonic solutions, where the time dependence of all fields goes as  $\mathbf{x} = \mathbf{x}_0 \exp(-i\omega t)$ , we can eliminate  $\mathbf{x} = -\gamma_{13}\mathbf{E}/(\omega^2 + \gamma_{11} + i\gamma_{12}\omega)$  from these equations, and relate  $\mathbf{P}$  and  $\mathbf{E}$  by the equation  $\mathbf{P} = [\gamma_{22} - \gamma_{13}^2/(\omega^2 + \gamma_{11} + i\gamma_{12}\omega)]\mathbf{E}$ . From the definition of the dielectric displacement,  $\mathbf{D} = \mathbf{E} + 4\pi\mathbf{P} = \epsilon\mathbf{E}$ , we obtain the dielectric function,  $\epsilon(\omega) = 1 + 4\pi\gamma_{22} - 4\pi\gamma_{13}^2/(\omega^2 + \gamma_{11} + i\gamma_{12}\omega)$ . If  $\epsilon(\omega)$  is written in terms of measurable quantities,

$$\epsilon(\omega) = \epsilon_\infty \left( 1 + \frac{\omega_p^2}{\omega_{TO}^2 - \omega^2 - i\gamma\omega} \right),$$

the  $\gamma$ -coefficients can be expressed as  $\gamma_{22} = (\epsilon_\infty - 1)/4\pi$ ,  $\gamma_{13} = (\epsilon_\infty/4\pi)^{1/2}\omega_p$ ,  $\gamma_{12} = \gamma$ , and  $\gamma_{11} = -\omega_{TO}^2$ .

Also notice that, neglecting the induced polarization in the ions (i.e., considering them as rigid), the coupling strength  $\omega_p$  can be estimated to be (42)

$$\omega_p = \sqrt{\frac{4\pi ne^2}{M}}. \quad (\text{S7})$$

## S7 Phonon polariton branches in a coaxial waveguide, for a single vibrational mode

Phonon polariton modes are obtained by solving both Maxwell and the dynamical lattice equations simultaneously. In this section we extend the theoretical framework summarized in Sec. S6 to the case of an infinite coaxial waveguide.

Let us consider a given waveguide mode M, characterized by a wavevector along the waveguide axes  $k$  (for instance  $M = TE_{11}$ , the fundamental mode of the coaxial waveguide described in Sec. S5). When the aperture is filled with a uniform dielectric constant  $\epsilon_\infty$  (originating from coupling to electronic degrees of freedom), the electric field satisfies the wave equation (S3)

$$\nabla \times \nabla \times E\mathbf{E}_M - \epsilon_\infty \frac{\omega_k^2}{c^2} E\mathbf{E}_M = 0,$$

where  $\mathbf{E} = E\mathbf{E}_M$  is electric-field vector with amplitude  $E$  and  $\mathbf{E}_M$  is the transverse solution of Maxwell equations for mode M at frequency  $\omega_k$ . When the phononic material fills the waveguide, the wave equation can be written in the general form

$$\nabla \times \nabla \times E\mathbf{E}_M - \frac{\omega^2}{c^2} (E + 4\pi P) \mathbf{E}_M = 0.$$

where P is the amplitude of polarization vector  $\mathbf{P} = P\mathbf{E}_M$ .  $\mathbf{E}_M$  satisfies both wave equations when the scaling relation (S5) is fulfilled, i.e.

$$\omega^2(E + 4\pi P) = \omega_k^2 E. \quad (\text{S8})$$

Sec. S5 shows it is a good approximation for the coaxial hole array studied experimentally.

We can also assume a local relation between  $\mathbf{E}$  and the displacement of charges  $\mathbf{x}(\mathbf{r})$ . Such assumption will be valid as long as the dispersion relation of the phonons is neglected, which is a good approximation because the  $k$  dependence of the uncoupled optical phonons is not usually very strong. Then, for a given mode profile,  $\mathbf{E}(\mathbf{r}) = E\mathbf{E}_M(\mathbf{r})$  and  $\mathbf{x}(\mathbf{r}) = x\mathbf{E}_M(\mathbf{r})$ , we

can employ the lattice equations described in Sec. S6,

$$-\omega^2 x = -\omega_{TO}^2 x + i\gamma\omega x + \sqrt{\frac{\epsilon_\infty}{4\pi}}\omega_p E, \quad (\text{S9})$$

$$P = \sqrt{\frac{\epsilon_\infty}{4\pi}}\omega_p x + \frac{\epsilon_\infty - 1}{4\pi} E. \quad (\text{S10})$$

Eliminating  $P$  from equations (S8-S10) the system of equations can be expressed in a matrix form, stating that  $\mathbf{E}_M(\mathbf{r}, \mathbf{k})$  is still a solution of Maxwell equations but at a frequency  $\omega$  satisfying

$$\begin{pmatrix} \omega^2 - \omega_{TO}^2 + i\gamma\omega & \omega\omega_p \\ \omega\omega_p & \omega^2 - \omega_k^2 + i\delta\omega_k \end{pmatrix} \cdot \begin{pmatrix} \omega x \\ \sqrt{\epsilon_\infty/4\pi} E \end{pmatrix} = 0,$$

where we have included a finite linewidth in the photon mode making the replacement  $\omega_k \rightarrow \omega_k - i\delta/2$ .

Nontrivial solutions for the homogeneous matrix equation developed in the main text exist only if the determinant of the matrix is set equal to zero. Assuming that  $\omega_{TO} \gg \omega_p \gg \gamma, \delta$  at the crossing point of the photon and TO phonon frequencies ( $\omega_k = \omega_{TO}$ ), we find from the secular equation that the degeneracy between the two modes is lifted,

$$\omega_\pm = \omega_{TO} \pm \frac{\omega_p}{2} - i\frac{\gamma_{FP} + \gamma}{4},$$

and the frequency splitting,  $\Delta\omega = \omega_+ - \omega_- = \omega_p$ , coincides with  $\omega_p$  in this simple case of one phonon mode. Moreover, the width of each dressed state is the average of the photon ( $\delta/2$ ) and phonon ( $\gamma/2$ ) linewidths. The splitting can be resolved only if  $\Delta\omega > (\gamma + \delta)/2$ .

Additional remarks:

- The frequency dependence of the coupling term is related to the long-range nature of the Coulomb forces (i.e the dipole-dipole interaction induced via an electric field), and does not appear in the text-book example of two harmonic oscillators (Sec. S11), due to the short-range nature of the oscillator restoring forces.



- The Reststrahlen band is smaller than the splitting, i.e  $\omega_{LO} - \omega_{TO} = (\omega_p/2\omega_{TO})\omega_p < \Delta\omega$ , and thus, the splitting is not simply the manifestation of absorption induced within the Reststrahlen band.
- The asymptotic limits of the general solution are

$$\begin{aligned}
\lim_{\omega'_k \rightarrow 0} \omega_- &= \omega_k \sqrt{\epsilon_\infty/\epsilon_0}, & \text{photon-like} \\
\lim_{\omega'_k \rightarrow 0} \omega_+ &= \omega_{LO}, & \text{phonon-like} \\
\lim_{\omega'_k \rightarrow \infty} \omega_- &= \omega_{TO}, & \text{phonon-like} \\
\lim_{\omega'_k \rightarrow \infty} \omega_+ &= \omega_k. & \text{photon-like}
\end{aligned}$$

The existence of 4 different asymptotes is a clear difference with respect to the case of two harmonic oscillators coupled with short-range interactions, which present only three asymptotic values (as the asymptotes represented by  $\omega_{TO}$  and  $\omega_{LO}$  would coincide in this case).

- The coupling strength is a function of the molecular concentration  $n$ ,  $\omega_p = \sqrt{4\pi n e^2 / M}$  (Eq. S7). The dependence  $\omega_p \sim \sqrt{n}$  is shared by classical, semi-classical and quantum descriptions (*I*). This behavior has been confirmed experimentally for a classical Fabry-Perot resonator (*43*).

## S8 Multiple vibrational degrees of freedom

The previous section discusses polaritonic branches in a coaxial waveguide filled with a material with a single vibrational optical mode. We consider now the influence of additional vibrational modes in the optical response of the filled coaxial aperture. The lattice equations of motion for

a unit cell with  $N$  oscillator normal modes read

$$\begin{aligned}
\ddot{x}_1 &= -\omega_{TO_1}^2 x_1 - \gamma_1 \dot{x}_1 + \sqrt{\frac{\epsilon_\infty}{4\pi}} \omega_{p_1} E, \\
\ddot{x}_2 &= -\omega_{TO_2}^2 x_2 - \gamma_2 \dot{x}_2 + \sqrt{\frac{\epsilon_\infty}{4\pi}} \omega_{p_2} E, \\
&\vdots \\
\ddot{x}_N &= -\omega_{TO_N}^2 x_N - \gamma_N \dot{x}_N + \sqrt{\frac{\epsilon_\infty}{4\pi}} \omega_{p_N} E, \\
P &= \sqrt{\frac{\epsilon_\infty}{4\pi}} \sum_{i=1}^N \omega_{p_i} x_i + \frac{\epsilon_\infty - 1}{4\pi} E.
\end{aligned}$$

Simultaneous solution of lattice and Maxwell's equations for transverse modes can be expressed as a matrix equation of order  $N + 1$ ,

$$\begin{pmatrix}
\omega^2 - \omega_{TO_1}^2 + i\gamma_1\omega & 0 & \dots & 0 & \omega\omega_{p_1} \\
0 & \omega^2 - \omega_{TO_2}^2 + i\gamma_2\omega & \dots & 0 & \omega\omega_{p_2} \\
\vdots & \vdots & \vdots & \vdots & \vdots \\
0 & 0 & \dots & \omega^2 - \omega_{TO_N}^2 + i\gamma_N\omega & \omega\omega_{p_N} \\
\omega\omega_{p_1} & \omega\omega_{p_2} & \dots & \omega\omega_{p_N} & \omega^2 - \omega_k'^2
\end{pmatrix} \cdot \mathbf{F} = 0, \tag{S11}$$

with  $\mathbf{F} = (\omega x_1, \omega x_2, \dots, \omega x_N, \sqrt{\epsilon_\infty/4\pi} E)^t$ . The secular equation for this matrix can be written as

$$\epsilon(\omega)\omega^2 = \omega_k^2,$$

provided that the effective dielectric function is generalized to include all vibrational modes,

$$\epsilon(\omega) = \epsilon_\infty \left( 1 + \sum_{j=1}^N \frac{\omega_{p_j}^2}{\omega_{TO_j}^2 - \omega^2 - i\gamma_j\omega} \right).$$

In Fig. S5, the experimental spectral position of transmission resonances for an array of coaxial holes filled with  $\text{SiO}_2$ , are compared with those calculated with the formalism described above. Calculations were done for two models for the dielectric constant of  $\text{SiO}_2$ : in one of them

we considered that only one vibrational mode contributed to  $\epsilon_{SiO_2}$ , while the other considered 3 vibrational modes (the contribution from each vibrational mode to  $\epsilon_{SiO_2}$  is described by a Lorentzian function using Palik's data (44)). For a single vibrational mode we find a good agreement with the upper band but the lower band is poorly described. The agreement with both bands is improved when two lower-frequency vibrational modes are added.

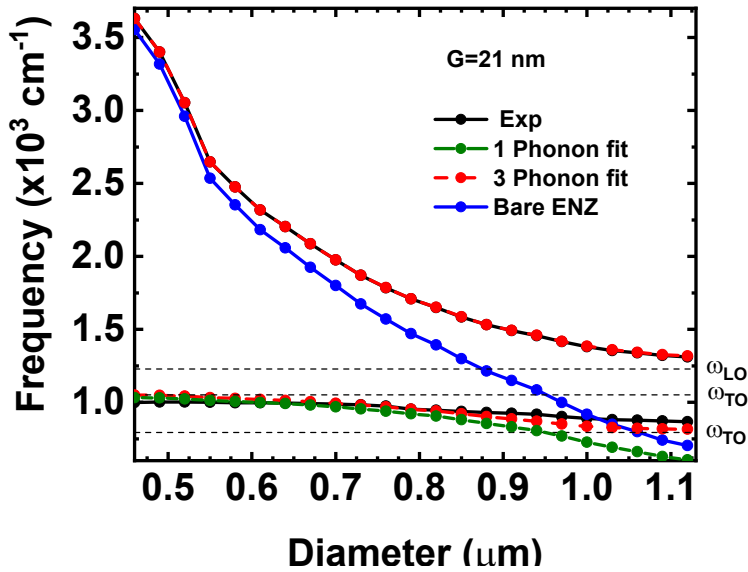


Figure S5: Experimental peak positions (black) for a coaxial gap of 21 nm filled with SiO<sub>2</sub> are compared with the fitted values for 1 (green) and 3 (red) vibrational modes as well as bare ENZ modes (blue).

## S9 Bulk phonon polaritons

Transverse waves in a homogeneous material also satisfy the propagation condition  $\epsilon(\omega)\omega^2 = \omega_k^2$ , where  $\omega_k = ck$ ,  $c$  is the speed of light and  $k$  the wavenumber of the plain wave. Following the approach outlined in Sec. S7, it is straightforward to show that bulk polaritonic modes are solution of the matrix equation (S11). Fig. S6 shows the polaritonics bands in bulk SiO<sub>2</sub> for three vibrational modes. Calculations are in agreement with experimental results of Ref. (45).

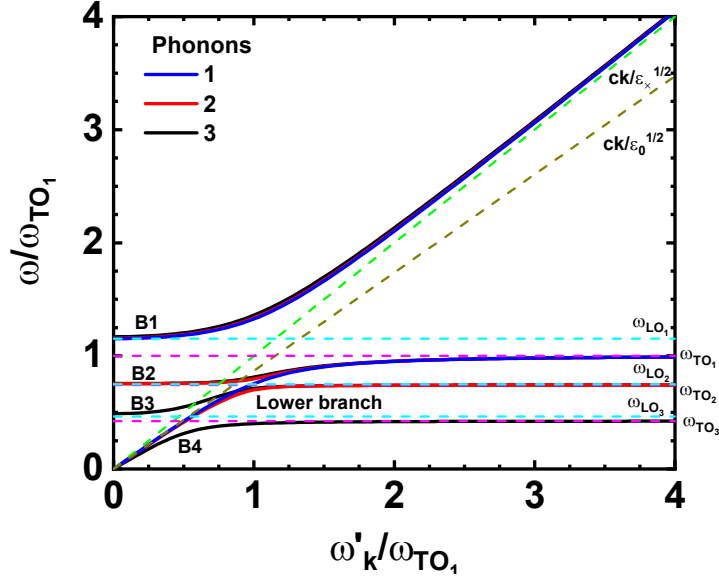


Figure S6: Dispersion relation of phonon polaritons for the vibrational modes of bulk SiO<sub>2</sub>.

## S10 Fitting experimental data to the cavity model

For a given coaxial array, filled with a phononic material, let us consider we have the spectral positions of the transmission resonances,  $\omega_i$ , for the  $N + 1$  polaritonic branches corresponding to the  $N$  vibrational modes and the fundamental waveguide mode. The fitting to the polaritonic dispersion relation,  $\omega^2\epsilon(\omega) = \omega_k^2$ , consists in the following two steps:

1. Extract the dispersion relation of the unfilled hole from the spectral positions:  $\omega_k = \omega_{i_0} \sqrt{\epsilon(\omega_{i_0})}$ . Notice that a single branch  $i_0$  is needed.
2. Solve the polynomial equation  $\omega^2\epsilon(\omega) = \omega_k^2$  for the remaining values of  $i$  in order to obtain the fitting frequencies.

Fig. S5 shows the results of the fitting for a coaxial gap of 21 nm filled with SiO<sub>2</sub>. Fitting with one and three vibrational modes are compared with experimental results.

## S11 Coupled harmonic oscillators

We consider two mechanical oscillators with eigenfrequencies  $\sqrt{k_A/m_A}$  and  $\sqrt{k_B/m_B}$  coupled by a spring with constant  $\kappa$  as a canonical example for strong coupling (46). The differential equations

$$\begin{aligned} m_A \ddot{x}_A + k_A x_A + \kappa (x_A - x_B) &= 0, \\ m_B \ddot{x}_B + k_B x_B - \kappa (x_A - x_B) &= 0, \end{aligned}$$

describe the motion of the system. The harmonic solutions of these equations can be written in a matrix form

$$\begin{pmatrix} \omega^2 - \omega_A^2 & \Gamma \\ \Gamma & \omega^2 - \omega_B^2 \end{pmatrix} \cdot \begin{pmatrix} \sqrt{m_A} x_A \\ \sqrt{m_B} x_B \end{pmatrix} = 0,$$

where  $\omega_A^2 = (k_A + \kappa)/m_A$ ,  $\omega_B^2 = (k_B + \kappa)/m_B$ , and  $\Gamma = \kappa/\sqrt{m_A m_B}$ . The diagonal terms contain the eigenfrequencies of the uncoupled oscillators, modified by the interaction, while the off-diagonal terms are proportional to the coupling strength. The secular equation yields the dressed frequencies of the system.

$$\omega_{\pm}^2 = \frac{\omega_A^2 + \omega_B^2 \pm \sqrt{(\omega_A^2 - \omega_B^2)^2 + 4\Gamma^2}}{2}.$$

The frequency splitting,  $\omega_+ - \omega_- \approx \Gamma$ , increases with the coupling strength. A numerical example is presented in Fig. S7.

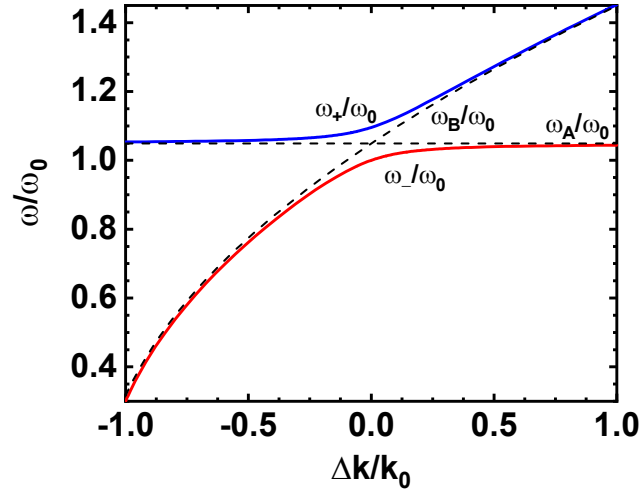


Figure S7: Bare (dashed lines) and dressed (solid lines) frequencies for a harmonic oscillator with  $\omega_A = \omega_0 \sqrt{1 + \kappa/k_0}$ ,  $\omega_B = \omega_0 \sqrt{1 + \Delta k/k_0 + \kappa/k_0}$ , and  $\kappa = 0.1 k_0$ .

## References and Notes

1. P. Törmä, W. L. Barnes, *Rep. Prog. Phys.* **78**, 013901 (2015).
2. T. W. Ebbesen, *Acc Chem Res* **49**, 2403 (2016).
3. A. F. Kockum, A. Miranowicz, S. D. Liberato, S. Savasta, F. Nori, *Nature Reviews Physics* **1**, 19–40 (2019).
4. M. Pelton, *Nature Photonics* **9**, 427–435 (2015).
5. B. Luk'yanchuk, *et al.*, *Nature Mater.* **9**, 707–715 (2010).
6. J. Vučković, M. Pelton, A. Scherer, Y. Yamamoto, *Phys. Rev. A* **66**, 023808 (2002).
7. T. Yoshie, *et al.*, *Nature* **432**, 200–203 (2004).
8. J. P. Reithmaier, *et al.*, *Nature* **432**, 197–200 (2004).

9. T. Aoki, *et al.*, *Nature* **443**, 671–674 (2006).
10. K. Santhosh, O. Bitton, L. Chuntonov, G. Haran, *Nature Commun.* **7**, 11823 (2016).
11. H. Leng, B. Szychowski, M.-C. Daniel, M. Pelton, *Nature Commun.* **9**, 4012 (2018).
12. H. Groß, J. M. Hamm, T. Tufarelli, O. Hess, B. Hecht, *Sci. Adv.* **4**, eaar4906 (2018).
13. K.-D. Park, *et al.*, *Sci. Adv.* **5**, eaav5931 (2019).
14. A. Shalabney, *et al.*, *Nature Commun.* **6**, 5981 (2015).
15. B. Munkhbat, M. Wers' all, D. G. Baranov, T. J. Antosiewicz, T. Shegai, *Sci. Adv.* **4**, eaas9552 (2018).
16. J. Feist, F. J. García-Vidal, *Phys. Rev. Lett.* **114**, 196402 (2015).
17. A. Thomas, *et al.*, *Science* **363**, 615 (2019).
18. H. J. Kimble, *Nature* **453**, 1023–1030 (2008).
19. P. Forn-Díaz, L. Lamata, E. Rico, J. Kono, E. Solano, *Rev. Mod. Phys.* **91**, 025005 (2019).
20. G. Romero, D. Ballester, Y. M. Wang, V. Scarani, E. Solano, *Phys. Rev. Lett.* **108**, 120501 (2012).
21. M. Ruggenthaler, N. Tancogne-Dejean, J. Flick, H. Appel, A. Rubio, *Nat Rev Chem.* **2**, 0118 (2018).
22. R. H. Dicke, *Phys. Rev.* **93**, 99–110 (1954).
23. F. Benz, *et al.*, *Science* **354**, 726 (2016).
24. F. Neubrech, C. Huck, K. Weber, A. Pucci, H. Giessen, *Chem. Rev.* **117**, 5110–5145 (2017).

25. S. Law, V. Podolskiy, D. W. Wasserman, *Nanophotonics* **2**, 103–130 (2013).
26. J. D. Caldwell, *et al.*, *Nanophotonics* **4**, 44–68 (2015).
27. E. A. Muller, *et al.*, *ACS Photonics* **5**, 3594–3600 (2018).
28. F. Neubrech, *et al.*, *Phys. Rev. Lett.* **101**, 157403 (2008).
29. X. G. Xu, M. Rang, I. M. Craig, M. B. Raschke, *J. Phys. Chem. Lett.* **3**, 1836–1841 (2012).
30. M. Autore, *et al.*, *Light : Science & Applications* **7**, 17172 (2018).
31. J. Lather, P. Bhatt, A. Thomas, T. W. Ebbesen, J. George, *Angew. Chem. Int. Ed.* **58**, 10635 (2019).
32. F. I. Baida, A. Belkhir, D. V. Labeke, O. Lamrous, *Phys. Rev. B* **74**, 205419 (2006).
33. D. Yoo, *et al.*, *Nano Lett* **16**, 2040 (2016).
34. A. Alù, N. Engheta, *Phys. Rev. B* **78**, 035440 (2008).
35. J. Kischkat, *et al.*, *Appl. Opt.* **51**, 6789 (2012).
36. M. Born, K. Huang, *Dynamical Theory of Crystal Lattices* (Oxford University Press, 1988).
37. R. J. Schoelkopf, S. M. Girvin, *Nature* **451**, 664 (2008).
38. J. D. Jackson, *Classical electrodynamics* (John Wiley, New York, 1999), third edn.
39. F. J. García-Vidal, L. Martín-Moreno, T. W. Ebbesen, L. Kuipers, *Rev. Mod. Phys.* **82**, 729 (2010).
40. F. de León-Pérez, G. Brucoli, F. J. García-Vidal, L. Martín-Moreno, *New J. Phys.* **10**, 105017 (2008).



41. K. Huang, *Proc. R. Soc. Lond. A* **208**, 352 (1951).
42. C. Kittel, *Quantum theory of solids* (John Wiley & Sons, New York, 1987), second edn.
43. Y. Zhu, *et al.*, *Phys. Rev. Lett.* **64**, 2499.
44. E. D. Palik, *Handbook of Optical Constants of Solids* (Academic, London, 1985).
45. J. Fries, R. Claus, *J. Raman Spect.* **1**, 71 (1973).
46. L. Novotny, B. Hecht, *Principles of Nano-optics* (Cambridge University Press, New York, 2006).